Tri-modality *in vivo* imaging for tumor detection with combined ultrasound, photoacoustic, and photoacoustic elastography

Shuaihu Wang [a,b], Bingxin Huang [a], Simon C.K. Chan [a], Victor T.C. Tsang [a], Terence T. W. Wong [a,c,*]

[a] *Translational and Advanced Bioimaging Laboratory, Department of Chemical and Biological Engineering, The Hong Kong University of Science and Technology, Hong Kong, China*
[b] *Department of Mechanical Engineering and Material Science, Washington University in St. Louis, St. Louis, MO 63130, USA*
[c] *Research Center for Medical Imaging and Analysis, The Hong Kong University of Science and Technology, Hong Kong, China*

ARTICLE INFO

ABSTRACT

A comprehensive understanding of a tumor is required for accurate diagnosis and effective treatment. However, currently, there is no single imaging modality that can provide sufficient information. Photoacoustic (PA) imaging is a hybrid imaging technique with high spatial resolution and detection sensitivity, which can be combined with ultrasound (US) imaging to provide both optical and acoustic contrast. Elastography can noninvasively map the elasticity distribution of biological tissue, which reflects pathological conditions. In this study, we incorporated PA elastography into a commercial US/PA imaging system to develop a tri-modality imaging system, which has been tested for tumor detection using four mice with different physiological conditions. The results show that this tri-modality imaging system can provide complementary information on acoustic, optical, and mechanical properties. The enabled visualization and dimension estimation of tumors can lead to a more comprehensive tissue characterization for diagnosis and treatment.

1. Introduction

Cancer remains one of the leading causes of mortality worldwide. As cancer advances, it experiences intricate pathological and biological changes, which exhibit notable variations among individuals, whose diagnosis and treatment need comprehensive information on its morphology, molecular composition, and biomechanical properties [1]. However, none of the existing standalone biomedical imaging methods can offer this extensive range of information. Therefore, hybrid or multi-modality approaches are important for precise diagnosis and personalized treatments.

Ultrasound (US) imaging is a widely used medical imaging modality that utilizes high-frequency sound waves to create real-time images of the internal structures of the body. However, its application in tumor detection is constrained by its poor sensitivity [2]. Photoacoustic (PA) tomography (PAT) is an emerging imaging technique that can provide label-free anatomical and functional contrast arising from intrinsic tissue components [3,4]. PAT combines the advantages of optical excitation and acoustic detection and overcomes the high degree of optical

photon scattering in biological tissue by making use of the PA effect, which is based on the generation of pressure waves upon absorption of optical energy [5,6]. This technique has been used for biomedical applications, including blood oxygenation and hemoglobin monitoring, and imaging of tumor angiogenesis [7–9]. Since both US and PA images are reconstructed based on the reception of US signals, which can be detected by the identical US transducer and receiving system, PA imaging can be easily integrated with the clinical US imaging system [10, 11]. Previous studies have established this dual-modality imaging system and proved its ability to provide complementary information about functional optical absorption spectra and acoustical morphological structure in biological tissues [11–13]. This compelling feature has driven the recent development of several commercial systems [10, 12–17].

The mechanical properties of biological tissues can provide insights into pathological conditions [18]. Elastography, an imaging technique that is based on existing medical imaging techniques, can map the distribution of mechanical properties in biological tissues [19]. Previous studies have integrated ultrasound elastography into US/PA imaging
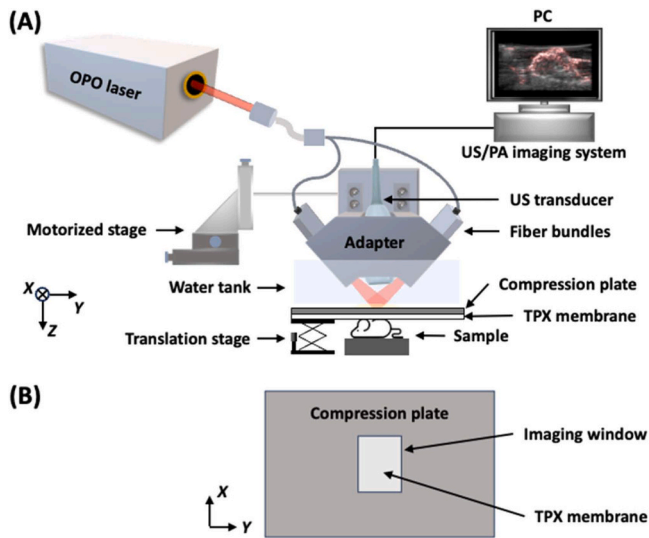
Fig. 1. Experimental setup. (A) Schematic of the proposed tri-modality imaging system. (B) Top view of the compression plate with the imaging window at the center. OPO, optical parametric oscillator; US, ultrasound; PC, personal computer; and TPX, polymethylpentene.

systems, specifically, strain elastography [20,21], shear wave elastography (SWE) [22,23], and acoustic radiation force impulse (ARFI) imaging [24]. These studies have proven that diverse imaging modalities could complement one another for more comprehensive tissue characterization. However, strain elastography is not suitable for some tumor detections because it relies on the comparison of US images before and after external deformation, and some tumors have low US signals. Additionally, SWE and ARFI require specific US transducers to generate shear waves (SWE) or emit high-intensity US pulses (ARFI), which are not always available.

PA elastography (PAE), implemented using PAT, is a high-resolution strain imaging technique based on the contrast of Young's modulus. PAE can map the mechanical contrast in biological tissue noninvasively while maintaining high spatial resolution and excellent penetration depth [25]. There have been several PA studies on measuring the elastic properties of biological tissue [25–28]. By adding a customized compression system, the PAT system can easily be modified to implement PAE, and the measurement of relative elastic properties and absolute map of Young's modulus have both been reported before, which proved the ability of PAE in measuring mechanical properties of biological tissues [25,26]. Wang et al. have proposed an approach for quantitative PA elasticity imaging, without external compression, by analyzing the rise time of the thermoelastic displacement [29], and integrated this method into the US/PA imaging system [30]. However, this method is limited to the superficial sample and requires specific US transducers equipped with ARFI techniques.

The primary objective of this paper is to integrate all three modalities (US/PA/PAE) based on a commercial US/PA imaging system, and investigate its ability in tumor detection. To this end, a tri-modality imaging method is proposed, and four mice with different physiological states are imaged and compared to demonstrate the viability of this tri-modality imaging method. The US, PA and PAE images obtained after image reconstruction enable the simultaneous assessment of optical features, echogenicity, and stiffness of the object, which can benefit tumor detection.

2. Methods

2.1. Experimental setup

Fig. 1A shows a schematic of the tri-modality imaging system that we developed based on a commercial US/PA imaging system (Acoustic X, CYBERDYNE INC., Japan). In this tri-modality system, the major component is a linear-array-based PA imaging probe, which consists of a linear array US transducer with two optical fiber bundle strips (with a 35 mm × 1 mm optical window for each) mounted on each side. The laser beams coming out of the two optical fiber bundle strips, which were bifurcated from a single optical bundle, were symmetrically aligned with respect to the US transducer axis both with an incident angle of 40 degrees. A tunable optical parametric oscillator (OPO) laser (NT352C-20-FWS-SH-H, EKSPLA, Inc.) was coupled for PA excitation. The excitation wavelength was set to 700 nm, where the laser system provides the highest energy per pulse and optimal optical window to achieve deep penetration. The laser pulse width was 3–5 ns and the repetition rate was 20 Hz. The fluence on the tissue surface was about 8.5 mJ/cm^2, below the 20 mJ/cm^2 safety limit set by the American National Standards Institute [31]. The US transducer has 128 individual elements, with each element having a transverse aperture of 5 mm and a pitch of 0.315 mm. The array has a focal length of 20 mm, a central frequency of 7 MHz, and a measured −6 dB bandwidth of 80 % [32]. The raw radiofrequency data from all elements are acquired at sampling rates of 20 MHz and 40 MHz for US and PA imaging, respectively, and then, transferred to the computer graphical processing unit board and reconstructed using a system-integrated Fourier transform analysis reconstruction algorithm [33] for real-time display. The lateral and axial resolutions of the system are ~309 µm and ~365 µm, respectively, which are confirmed by measuring the respective point spread functions using a human black hair (Supplementary Figure S1).

To implement PAE, a customized compression stage was developed and incorporated into the system. The compression stage is composed of an aluminum plate, a polymethylpentene (TPX) plastic membrane, and a translation stage. The aluminum plate, with an imaging window slightly larger than the probe, was controlled by the manual translation stage, which could induce precise displacements (minimum of 10 µm) along the Z-axis for sample compression. A piece of fully stretched TPX plastic membrane is attached to the bottom of the compression plate, as shown in Fig. 1B, to ensure the compression force applied to the sample is normal and uniaxial, and it allows the transmission of both the excitation light and the generated PA wave. Above the compression plate, a water tank holds water for acoustic coupling. US gel is used for acoustic coupling between the compression plate and both the water tank and the sample.

2.2. Animal preparation

Four BALB/c mice were imaged in this study (healthy, with agarose implanted, with a big tumor, and with a small tumor). All studies were approved by the Animal Ethics Committee at The Hong Kong University of Science and Technology.

2.2.1. Agarose implanted mouse model

Carbon powder, with an average diameter of 50 µm, was mixed in the 1.5 % agarose solution at a concentration of approximately 5 particles per mm^3 to create the agarose phantom, measuring 5 mm in diameter and 4.5 mm in thickness. The implantation of the agarose phantom was performed under full anesthesia with ~1.5 % isoflurane mixed with oxygen at a flow rate of 0.6 L/min using an endotracheal tube during the surgery. A roughly 1 cm incision was made on the dorsal side of the mouse, after which a subcutaneous pocket was prepared by blunt dissection. Then, the agarose phantom was inserted into the subcutaneous pocket. Following this, the incision was meticulously closed by surgical suture. After a healing period of 3 days, the mouse was used for *in vivo* experiment.

2.2.2. 4T1 cell allograft mouse model

The mouse breast cancer 4T1 cell line, obtained from the American Type Culture Collection (ATCC, Manassas, VA, USA), was cultivated in
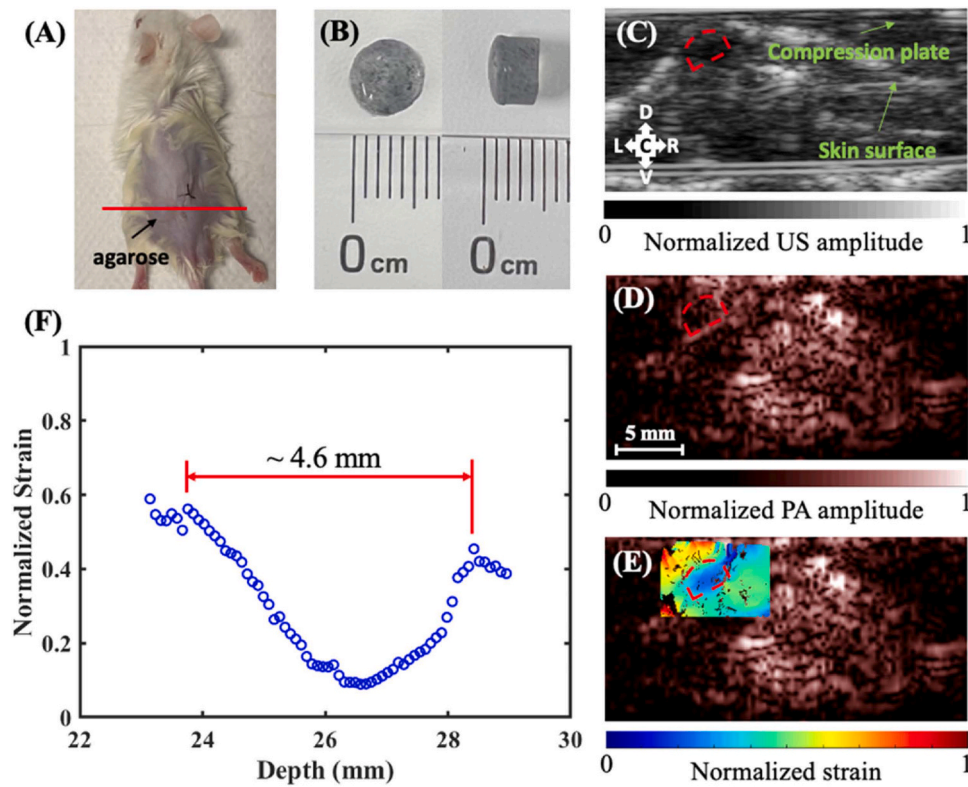
Fig. 2. Cross-sectional images by the three imaging modalities of a mouse with agarose implantation. (A) Photograph of the mouse with agarose implantation. The red line shows the imaging slice position. (B) Top view and side view of the agarose phantom implanted. (C) US cross-sectional image. (D) PA cross-sectional image. (E) Normalized strain measurement by PAE superimposed on the structural PA image. The red dashed line shows the position of agarose in images. (F) Normalized strain versus depth. DV: dorsal-ventral; RC: rostral-caudal; RL: right-left.

RPMI 1640 medium supplemented with 10 % fetal bovine serum and 1 % penicillin-streptomycin solution. The cells were cultured in a 5 % carbon dioxide (CO_2) incubator at 37°C. Subconfluent 4T1 cells were trypsinated and suspended in phosphate-buffered saline (PBS). A cell resuspension with a cell density of 1×10^6 cells/mL was prepared in PBS for subsequent injection.

To establish the 4T1 cell allograft mouse model, female BALB/c mice (Bagg Albino Laboratory-bred mice, c strain) aged 6–8 weeks and weighing 30–35 g were utilized. The hair surrounding the injection site (the left abdominal mammary gland) was removed using clippers. This area was then sterilized through three alternating swabs of betadine and 70 % ethanol. Subsequently, 200 μL of 4T1 cells (2×10^5 cells) was subcutaneously injected using a 1 mL tuberculin syringe equipped with a 27-gauge needle. After one week, a palpable primary tumor had formed and was monitored, referred to a mouse with a small tumor. Three to four weeks following the injection of 4T1 cells, the tumor size had significantly increased when referred to a mouse with a big tumor.

2.3. Image acquisition

The performance of the tri-modality imaging system was investigated in all four mice. For each experiment, the mouse was anesthetized with ~1.5 % isoflurane mixed with oxygen at a flow rate of 0.6 L/min using an endotracheal tube during the imaging. The anesthetized mouse was fixed on the object holder in the ventral decubitus position and imaged by this tri-modality imaging system. A cross-section of the mouse was first imaged right after the compression plate contacted the back of the mouse with a minimum load. Since the compression plate cannot maintain continuous contact with the whole back of the mouse, we only ensure that the compression plate remains in contact with the region of interest during the experiment, for example, the agarose implanted or tumor. Then, we applied a compression of 200 μm, which

led to a maximum strain of less than 5 % and thus was considered to be within the linear strain response regime. The US and PA images were acquired after this compression.

For mice with tumors, the mice were sacrificed with CO_2 narcosis and asphyxiation after imaging. The tumor tissues were extracted and fixed in 4 % neutral-buffered formalin at room temperature for 24 hours. After fixation, the extracted tissues were processed for dehydration and paraffin infiltration with a tissue processor (Revos, Thermo Fisher Scientific, Inc.) for nearly 12 hours. Then, the tissues were embedded into paraffin blocks and subsequently sectioned into 5 μm thin slices by a microtome. Finally, the sectioned thin slices were mounted on glass slides, stained by hematoxylin and eosin (H&E), and imaged by a whole-slide scanner (Nanozoomer-SQ C13140, Hamamatsu Photonics K.K.) to obtain the histological images of tumor tissues.

2.4. Strain calculation

Strain values of the four mice under compression were obtained by analyzing the reconstructed B-scan PA images before and after compression. Here, cross-correlation was computed between the cross-sectional PA images before and after compression using Ncorr [34] to find the displacement in the Z-direction. Multiple images were acquired within a respiratory interval, and images before and after compression captured during similar respiratory phases were selected for the cross-correlation. The strain image was then obtained by numerically differentiating the displacements, as $\varepsilon_z = \frac{\partial w}{\partial z}$, assuming that the applied compression was uniaxial. The normalized strain fields, $\varepsilon_{z\,normalized} = \frac{\varepsilon_z - \varepsilon_{z\,min}}{\varepsilon_{z\,max} - \varepsilon_{z\,min}}$, were then masked for the region of interest and averaged at each depth. The detailed method and an example of the normalized strain calculation are shown in the Supplementary Material.
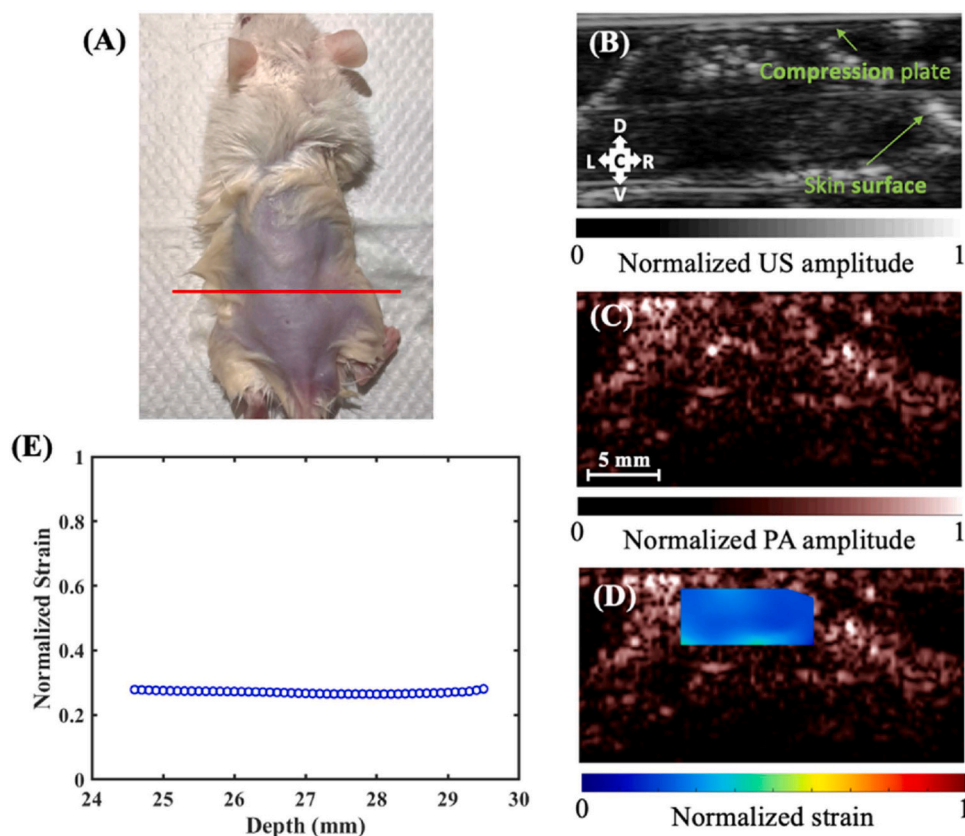
Fig. 3. Cross-sectional images by the three imaging modalities of a healthy mouse. (A) Photograph of the mouse. The red line shows the imaging slice position. (B) US cross-sectional image. (C) PA cross-sectional image. (D) Normalized strain measurement by PAE superimposed on the structural PA image. (E) Normalized strain versus depth.

3. Results

To evaluate the tri-modality imaging performance, a mouse with agarose implanted is imaged, as shown in Fig. 2A. Fig. 2C shows the cross-sectional US image (the red dashed line shows the position of agarose implanted), which is a hypoechoic inclusion and thus forms a relatively dark region. Due to the presence of carbon powder mixed in the agarose phantom, the PA signals in the corresponding region in the PA image can be observed (Fig. 2D). The normalized strain image was superimposed on the structural PA image, as shown in Fig. 2E. The region of the agarose phantom with a smaller strain was stiffer than the surrounding region of the mouse's tissue. Near the top and bottom boundaries of the agarose phantom, relatively high strain regions were observed because a high concentration of strain (or stress) will appear in areas where there is a significant change in stiffness. The normalized strain field was averaged at each depth, and the abrupt change can be observed in Fig. 2F. The size of this stiffer inclusion can be estimated, which is about 4.6 mm and aligns with the dimension of the agarose phantom (Fig. 2B).

As a comparative case to confirm the ability of this tri-modality imaging method, a healthy mouse without any interventions is imaged, as shown in Fig. 3. There is no obvious difference between the mouse with and without agarose implantation in the US image (Fig. 3B) and the PA image (Fig. 3C). In contrast, the relatively uniform PAE image (Fig. 3D) and line profile of averaged normalized strain approximating a straight line (Fig. 3E), compared to Fig. 2E and F, respectively, proves that PAE, and thus this tri-modality imaging method, has the capability to distinguish abnormal inclusion from normal tissues.

To evaluate the ability of the tri-modality imaging method for tumor detection, a mouse with a big tumor is imaged, as shown in Fig. 4. The tumor is usually hypoechoic, which is relatively dark in the US image

(Fig. 4C). Tumors require a blood supply to support their rapid growth, as a result, they often have a high density of blood vessels, which generate strong PA signals, as shown in Fig. 4D. Similar to the PAE image of the mouse with agarose implantation, since the tumor is stiffer than the surrounding tissues, there is a small strain region in the predicted position of the tumor, and the high concentration of strain is also observed near the top and bottom boundaries of the tumor (Fig. 4E). The irregular shape of the normalized strain map was due to incomplete contact between the compression plate and the back of the mouse, which resulted in the missing estimations of displacement in those areas and consequently missing the strain field. The normalized strain field was averaged at each depth, and the size of this tumor can be estimated from the line profile (Fig. 4F), which is about 4.5 mm. The estimated dimension of this tumor is consistent with those measured from the H&E-stained image of the dissected tumor (Fig. 4B), with a difference of approximately 6 %.

To further assess the performance of the tri-modality imaging method in detecting tumors of various sizes, we imaged another mouse with a smaller tumor compared to what is shown in Fig. 4, as illustrated in Fig. 5. From the H&E-stained image of the dissected tumor (Fig. 5B), it can be observed that this tumor is primarily composed of tissue resembling fat, and the degree of malignancy is relatively low. Therefore, no obvious structural and mechanical change was expected in this tumor. In Fig. 5C, the relatively dark region near the predicted position of the tumor can be observed since both fat and tumor are usually hypoechoic. There are PA signals near the predicted position of the tumor in Fig. 5D, and some relatively weak contrasts can be observed in the PAE image (Fig. 5E). The normalized strain field was averaged at each depth. In the line profile (Fig. 5F), it can be observed that the strain gradually decreased with depth, followed by a gradual increment. However, based on the information provided, the size of the tumor cannot be
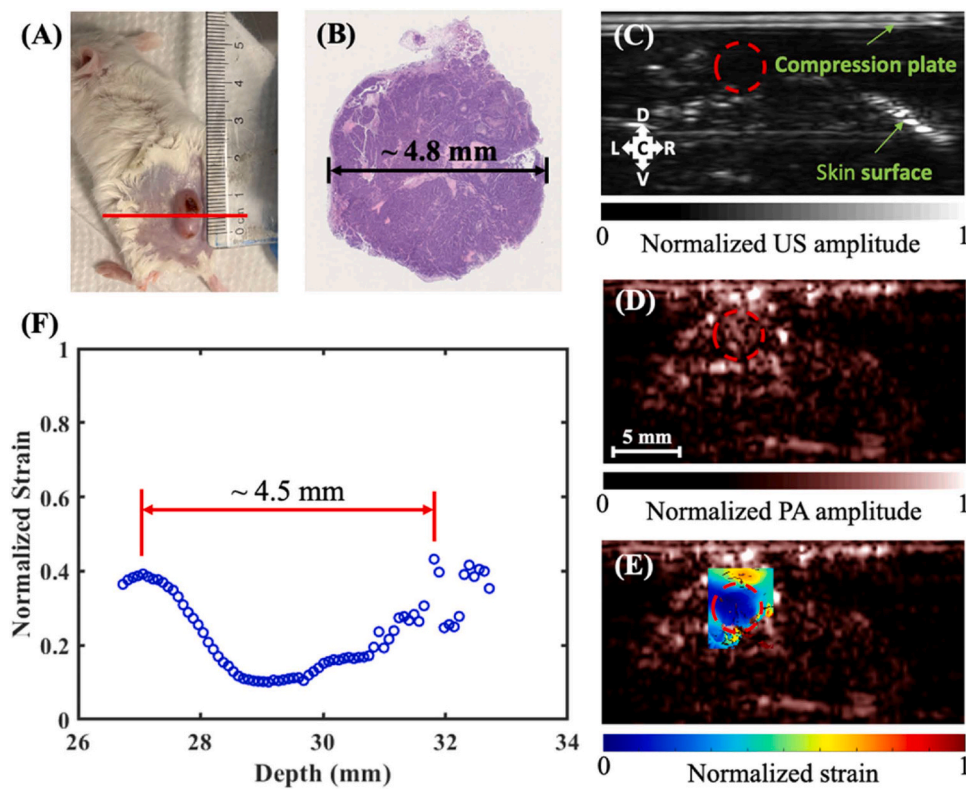
Fig. 4. Cross-sectional images by the three imaging modalities of a mouse with a big tumor. (A) Photograph of the mouse with a big tumor. The red line shows the imaging slice position. (B) H&E-stained image of the dissected tumor. (C) US cross-sectional image. (D) PA cross-sectional image. (E) Normalized strain measurement by PAE superimposed on the structural PA image. The red dashed line shows the position of the tumor in images. (F) Normalized strain versus depth.

Fig. 5. Cross-sectional images by the three imaging modalities of a mouse with a small tumor. (A) Photograph of the mouse with a small tumor. The red line shows the imaging slice position. (B) H&E-stained image of the dissected tumor. (C) US cross-sectional image. (D) PA cross-sectional image. (E) Normalized strain measurement by PAE superimposed on the structural PA image. The red dashed line shows the position of the tumor in images. (F) Normalized strain versus depth.
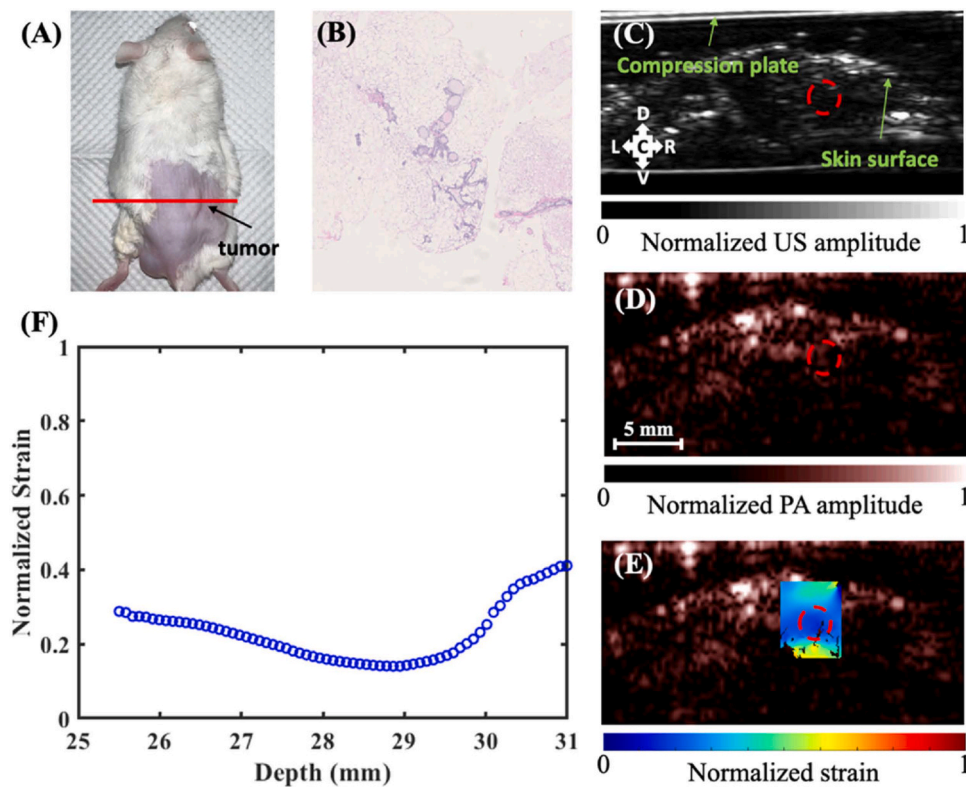
determined.

4. Discussion

By combining US, PA, and PAE, we introduced a tri-modality imaging method and assessed its effectiveness in tumor detection. This imaging method is significantly different from the previous tri-modality system [20–24], with respect to imaging mechanisms. Specifically, the elastography in our method is obtained based on the PA effect. US and PA signals can be acquired in parallel, and US, PA, and PAE data are exactly co-registered since they use the same US transducer. We imaged four mice with different physiological states: a healthy mouse, a healthy mouse with agarose implantation, a mouse with a big tumor, and a mouse with a small tumor. When comparing healthy mice with or without agarose implantation, noticeable differences were observed, especially in the PAE results. This suggests that this tri-modality system possesses the capability to identify hard inclusion. Images acquired in the mouse with a big tumor also show the efficacy of this tri-modality system in the context of tumor detection. The dimension estimation difference for the agarose implanted and the big tumor were both about 6 %, underscoring the relatively high precision of this imaging system. However, when imaging the mouse with a small tumor, the results were not as ideal as the big tumor for size estimation. The reason is that this small tumor is mainly composed of fat, and its degree of malignancy is not that high, which makes the changes in tissue properties not pronounced and leads to low contrast in images. These results show that, by incorporating PAE into the US/PA system, this tri-modality imaging method can provide more comprehensive information, which is significant in tumor detection and dimension estimation.

In addition, we acknowledge several limitations of this study. First, a flat compression plate was utilized in this study, which results in incomplete contact between the plate and the curved tissue surface, and leads to an irregular shape of normalized strain results. In the future, it is possible to design a specialized compression system for curved tissue surfaces, which can enable us to apply normal uniform compression force. A single optical wavelength was used in this study. Future studies should also include other wavelengths to provide more structural and functional information on different biomolecules. Additionally, only cross-sectional images were shown in this study. Volumetric imaging can be achieved by using a motorized probe and incorporating a proper registration algorithm, which can provide us with more valuable information in three dimensions. Another limitation of this study is that PAE was performed qualitatively with a simple compression plate, where only normalized strain maps were obtained to indicate the relative difference within a narrow region. Quantitative PAE can be achieved by adding a stress sensor on the compression plate to generate the stiffness map, along with a special compression mechanism, which can allow us to achieve mapping of the absolute Young's modulus *in vivo*.

5. Conclusion

To the best of our knowledge, this study is the first one to propose a tri-modality imaging method that combines US, PA, and PAE in tumor detection *in vivo*. A tunable OPO laser and a customized compression stage were incorporated into a commercial US/PA imaging system to build this tri-modality imaging system. Four mice with different physiological states were imaged using this system to investigate its ability in tumor detection. The current results reveal that this imaging method can provide complementary information on optical, acoustic, and mechanical properties, which benefits tumor detection and even tumor dimension estimation. These promising results motivate further development of this system for clinical applications.

CRediT authorship contribution statement

Victor T. C. Tsang: Resources, Investigation. **Terence T. W. Wong:** Writing – review & editing, Supervision, Resources, Project administration, Funding acquisition, Conceptualization. **Bingxin Huang:** Writing – review & editing, Visualization, Validation, Resources, Investigation, Data curation. **Simon C. K. Chan:** Software, Investigation, Formal analysis, Data curation. **Shuaihu Wang:** Writing – review & editing, Writing – original draft, Visualization, Validation, Software, Methodology, Investigation, Formal analysis, Data curation, Conceptualization.

Declaration of Competing Interest

The authors declare the following financial interests/personal relationships which may be considered as potential competing interests: Terence T. W. Wong has a financial interest in PhoMedics Limited, which, however, did not support this work. Other authors declare that they have no known competing financial interests or personal relationships that could have appeared to influence the work reported in this paper.

Data Availability

Data will be made available on request.

Appendix A. Supporting information

Supplementary data associated with this article can be found in the online version at doi:10.1016/j.pacs.2024.100630.

References

[1] A.A. Alizadeh, V. Aranda, A. Bardelli, C. Blanpain, C. Bock, C. Borowski, C. Caldas, A. Califano, M. Doherty, M. Elsner, M. Esteller, R. Fitzgerald, J.O. Korbel, P. Lichter, C.E. Mason, N. Navin, D. Pe'er, K. Polyak, C.W.M. Roberts, L. Siu, A. Snyder, H. Stower, C. Swanton, R.G.W. Verhaak, J.C. Zenklusen, J. Zuber, J. Zucman-Rossi, Toward understanding and exploiting tumor heterogeneity, Nat. Med. 21 (2015) 846–853, https://doi.org/10.1038/nm.3915.

[2] R. Guo, G. Lu, B. Qin, B. Fei, Ultrasound imaging technologies for breast cancer detection and management: a review, Ultrasound Med. Biol. 44 (2018) 37–70, https://doi.org/10.1016/j.ultrasmedbio.2017.09.012.

[3] J. Yao, J. Xia, K.I. Maslov, M. Nasiriavanaki, V. Tsytsarev, A.V. Demchenko, L. V. Wang, Noninvasive photoacoustic computed tomography of mouse brain metabolism in vivo, NeuroImage 64 (2013) 257–266, https://doi.org/10.1016/j.neuroimage.2012.08.054.

[4] L.V. Wang, Multiscale photoacoustic microscopy and computed tomography, Nat. Photonics 3 (2009) 503–509, https://doi.org/10.1038/nphoton.2009.157.

[5] L.V. Wang, S. Hu, Photoacoustic tomography: in vivo imaging from organelles to organs, Science 335 (2012) 1458–1462, https://doi.org/10.1126/science.1216210.

[6] L.V. Wang, Tutorial on photoacoustic microscopy and computed tomography, IEEE J. Sel. Top. Quantum Electron. 14 (2008) 171–179, https://doi.org/10.1109/JSTQE.2007.913398.

[7] M. Li, Y. Tang, J. Yao, Photoacoustic tomography of blood oxygenation: A mini review, Photoacoustics 10 (2018) 65–73, https://doi.org/10.1016/j.pacs.2018.05.001.

[8] G. Ku, X. Wang, X. Xie, G. Stoica, L.V. Wang, Imaging of tumor angiogenesis in rat brains in vivo by photoacoustic tomography, Appl. Opt. 44 (2005) 770–775, https://doi.org/10.1364/AO.44.000770.

[9] X. Wang, Y. Pang, G. Ku, X. Xie, G. Stoica, L.V. Wang, Noninvasive laser-induced photoacoustic tomography for structural and functional in vivo imaging of the brain, Nat. Biotechnol. 21 (2003) 803–806, https://doi.org/10.1038/nbt839.

[10] C. Kim, T.N. Erpelding, L. Jankovic, L.V. Wang, Performance benchmarks of an array-based hand-held photoacoustic probe adapted from a clinical ultrasound system for non-invasive sentinel lymph node imaging, Philos. Trans. A Math. Phys. Eng. Sci. 369 (2011) 4644–4650, https://doi.org/10.1098/rsta.2010.0353.

[11] J. Kim, S. Park, Y. Jung, S. Chang, J. Park, Y. Zhang, J.F. Lovell, C. Kim, Programmable real-time clinical photoacoustic and ultrasound imaging system, Sci. Rep. 6 (2016) 35137, https://doi.org/10.1038/srep35137.

[12] C. Lee, W. Choi, J. Kim, C. Kim, Three-dimensional clinical handheld photoacoustic/ultrasound scanner, Photoacoustics 18 (2020) 100173, https://doi.org/10.1016/j.pacs.2020.100173.

[13] T.N. Erpelding, C. Kim, M. Pramanik, L. Jankovic, K. Maslov, Z. Guo, J.A. Margenthaler, M.D. Pashley, L.V. Wang, Sentinel lymph nodes in the rat: noninvasive photoacoustic and US imaging with a clinical US system1, Radiology 256 (2010) 102–110, https://doi.org/10.1148/radiol.10091772.

[14] D.A. Tsyboulski, A.V. Liopo, R. Su, S.A. Ermilov, S.M. Bachilo, R.B. Weisman, A.A. Oraevsky, Enabling in vivo measurements of nanoparticle concentrations with three-dimensional optoacoustic tomography, J. Biophotonics 7 (2014) 581–588, https://doi.org/10.1002/jbio.201200233.

[15] J. Joseph, M.K. Ajith Singh, N. Sato, S.E. Bohndiek, Technical validation studies of a dual-wavelength LED-based photoacoustic and ultrasound imaging system, Photoacoustics 22 (2021) 100267, https://doi.org/10.1016/j.pacs.2021.100267.

[16] J. Yuan, G. Xu, Y. Yu, Y. Zhou, P.L. Carson, X. Wang, X. Liu, Real-time photoacoustic and ultrasound dual-modality imaging system facilitated with graphics processing unit and code parallel optimization, J. Biomed. Opt. 18 (2013) 086001, https://doi.org/10.1117/1.JBO.18.8.086001.

[17] A. Needles, A. Heinmiller, J. Sun, C. Theodoropoulos, D. Bates, D. Hirson, M. Yin, F.S. Foster, Development and initial application of a fully integrated photoacoustic micro-ultrasound system, IEEE Trans. Ultrason. Ferroelectr. Freq. Control 60 (2013) 888–897, https://doi.org/10.1109/TUFFC.2013.2646.

[18] J.F. Greenleaf, M. Fatemi, M. Insana, Selected methods for imaging elastic properties of biological tissues, Annu. Rev. Biomed. Eng. 5 (2003) 57–78, https://doi.org/10.1146/annurev.bioeng.5.040202.121623.

[19] A. Manduca, T.E. Oliphant, M.A. Dresner, J.L. Mahowald, S.A. Kruse, E. Amromin, J.P. Felmlee, J.F. Greenleaf, R.L. Ehman, Magnetic resonance elastography: noninvasive mapping of tissue elasticity, Med. Image Anal. 5 (2001) 237–254, https://doi.org/10.1016/s1361-8415(00)00039-6.

[20] S.Y. Emelianov, S.R. Aglyamov, J. Shah, S. Sethuraman, W.G. Scott, R. Schmitt, M. Motamedi, A. Karpiouk, A.A. Oraevsky, Combined ultrasound, optoacoustic, and elasticity imaging. Photons Plus Ultrasound Imaging Sens., SPIE, 2004, pp. 101–112, https://doi.org/10.1117/12.537155.

[21] S. Park, S.R. Aglyamov, W.G. Scott, S.Y. Emelianov, S. Sethuraman, J.M. Rubin, J. Shah, A.B. Karpiouk, S. Mallidi, R.W. Smalling, Synergy and applications of combined ultrasound, elasticity, and photoacoustic imaging, IEEE Ultrason. Symp. 2006 (2006) 405–415, https://doi.org/10.1109/ULTSYM.2006.114.

[22] H. Yoon, Y.I. Zhu, S.K. Yarmoska, S.Y. Emelianov, Design and demonstration of a configurable imaging platform for combined laser, ultrasound, and elasticity imaging, IEEE Trans. Med. Imaging 38 (2019) 1622–1632, https://doi.org/10.1109/TMI.2018.2889736.

[23] E. Zheng, H. Zhang, W. Hu, M.M. Doyley, J. Xia, Volumetric tri-modal imaging with combined photoacoustic, ultrasound, and shear wave elastography, J. Appl. Phys. 132 (2022) 034902, https://doi.org/10.1063/5.0093619.

[24] C.D. Nguyen, Y. Chen, D.L. Kaplan, S. Mallidi, Multi-spectral photoacoustic imaging combined with acoustic radiation force impulse imaging for applications in tissue engineering, (2024) 2024.04.23.590806. https://doi.org/10.1101/2024.04.23.590806.

[25] P. Hai, J. Yao, G. Li, C. Li, L.V. Wang, Photoacoustic elastography, Opt. Lett. 41 (2016) 725–728.

[26] P. Hai, Y. Zhou, L. Gong, L.V. Wang, Quantitative photoacoustic elastography in humans, J. Biomed. Opt. 21 (2016) 66011, https://doi.org/10.1117/1.JBO.21.6.066011.

[27] P. Hai, Y. Zhou, J. Liang, C. Li, L.V. Wang, Photoacoustic tomography of vascular compliance in humans, J. Biomed. Opt. 20 (2015) 126008, https://doi.org/10.1117/1.JBO.20.12.126008.

[28] Y. Zhao, S. Yang, C. Chen, D. Xing, Simultaneous optical absorption and viscoelasticity imaging based on photoacoustic lock-in measurement, Opt. Lett. 39 (2014) 2565–2568, https://doi.org/10.1364/OL.39.002565.

[29] Q. Wang, Y. Shi, F. Yang, S. Yang, Quantitative photoacoustic elasticity and viscosity imaging for cirrhosis detection, Appl. Phys. Lett. 112 (2018) 211902, https://doi.org/10.1063/1.5021675.

[30] P. Wang, Z. Chen, F. Yang, S. Yang, D. Xing, Intravascular tri-modality system: combined ultrasound, photoacoustic, and elasticity imaging, Appl. Phys. Lett. 113 (2018) 253701, https://doi.org/10.1063/1.5051387.

[31] (ANSI) American National Standard Institute Inc, ANSI Z136.1-2007: American National Standard for Safe Use of Lasers, (2007).

[32] A. Hariri, J. Lemaster, J. Wang, A.S. Jeevarathinam, D.L. Chao, J.V. Jokerst, The characterization of an economic and portable LED-based photoacoustic imaging system to facilitate molecular imaging, Photoacoustics 9 (2018) 10–20, https://doi.org/10.1016/j.pacs.2017.11.001.

[33] K.P. Köstli, P.C. Beard, Two-dimensional photoacoustic imaging by use of Fourier-transform image reconstruction and a detector with an anisotropic response, Appl. Opt. 42 (2003) 1899–1908, https://doi.org/10.1364/AO.42.001899.

[34] J. Blaber, B. Adair, A. Antoniou, Ncorr: open-source 2D digital image correlation matlab software, Exp. Mech. 55 (2015) 1105–1122, https://doi.org/10.1007/s11340-015-0009-1.

Shuaihu Wang received his B.Eng. degree in 2017 and M. Eng. degree in 2020 in Mechanical Engineering from Harbin Engineering University, China. He is currently a Ph.D. candidate in Mechanical Engineering, Washington University in St. Louis, United States. His research interests include elastography and biomechanics.

Bingxin Huang received her B.Eng. degree from Xi'an Jiaotong University, Xi'an, China. Currently, she is pursuing her PhD degree in Bioengineering, Hong Kong University of Science and Technology (HKUST), Hong Kong, China. Her research interests include low-cost and compact devices for biomedical imaging.

Simon C. K. Chan received his B.Eng. degree in Electronic Engineering from the Hong Kong University of Science and Technology (HKUST) in 2021. He continued his academic journey at HKUST, obtaining an M.Phil. in Bioengineering in 2023. He is currently a Ph.D. candidate in Bioengineering at the same institution. His research interests are focused on the application of deep learning algorithms to medical imaging, particularly in photoacoustic imaging and image reconstruction. Simon is dedicated to advancing the accuracy and efficiency of medical diagnostics through cutting-edge imaging technologies.

Victor T. C. Tsang obtained his B.Sc in Chemistry in 2019 and M.Phil. in Bioengineering in 2021 in HKUST. He is currently a Ph.D. student in the Department of Chemical and Biological Engineering at HKUST, majoring in bioengineering under the support of Hong Kong Ph.D. Fellowship scheme. His research interests are mainly on developing safe contrast agents for different imaging modalities.

Terence T. W. Wong is an assistant professor at HKUST and a director of the HKUST Research Center for Medical Imaging and Analysis. He received his Ph.D. degree from Washington University in St. Louis and California Institute of Technology. He has published over 50 publications in top peer-reviewed journals and conference papers. His research interests are smart optical and photoacoustic devices for label-free and high-speed histological imaging, three-dimensional whole-organ imaging, and low-cost cancer-targeting deep-tissue imaging.